Materials Chemistry and Physics 140 (2013) 49–59

Contents lists available at SciVerse ScienceDirect

Materials Chemistry and Physics

journal homepage: www.elsevier.com/locate/matchemphys

Synthesis and characterization of WO_3 thin films by surfactant assisted spray pyrolysis for electrochromic applications

L.M. Bertus [a], C. Faure [b], A. Danine [b], C. Labrugere [c], G. Campet [b], A. Rougier [b], A. Duta [a,*]

[a] The RTD Center Renewable Energy Systems and Recycling, Transilvania University of Brasov, Eroilor 29, 500036 Brasov, Romania
[b] CNRS, Université de Bordeaux, ICMCB, 87 Avenue du Dr. Albert Schweitzer, F-33608 Pessac, France
[c] CeCaMA, Université de Bordeaux, ICMCB, 87 Avenue du Dr. A. Schweitzer, F-33608 Pessac, France

HIGHLIGHTS

- WO_3 thin films obtained by surfactant/polymer mediated spray pyrolysis.
- Solvation/interaction of WCl_6 in/with surfactant changed solution properties.
- Film growth, crystallinity and topography influenced by solution composition.
- Film moisture sensitivity/wettability increased with surfactant content.
- Electrochromic activity of templated WO_3 films tested in ionic liquid.

ARTICLE INFO

Article history:
Received 30 June 2012
Received in revised form
31 January 2013
Accepted 18 February 2013

Keywords:
Optical materials
Chemical synthesis
Electrochemical techniques
Surface properties

ABSTRACT

Thin films of WO_3 were prepared by surfactant assisted spray pyrolysis on F-doped SnO_2 (FTO) conductive glass by using hexadecyltrimethylammonium bromide (HTAB) and polyethylene glycol (PEG400):HTAB as growth controlling agents. The surface tension of the spraying solutions was experimentally evaluated and was correlated with the deposition processes (nucleation and growth) of very smooth and homogenous films. The effect of the surfactant, alone and associated with PEG, on the structure (XRD), morphology (AFM), surface composition (XPS), FTIR and hydrophilicity (contact angle) were investigated and their influence on the electrochromic activity was discussed. Using surfactants and PEG, the coloration efficiency, transmission modulation and cycling stability of the WO_3 thin films can be enhanced.

1. Introduction

The electrochromic performance of tungsten oxide (WO_3) depends on its structure and morphology. Although physical methods have the advantage of excellent control over the layer's properties, the wet chemical routes such as electrodeposition, sol–gel dip/spin coating or spray pyrolysis deposition (SPD) have the advantage of lower costs and high deposition areas. These techniques allow a flexible selection of the precursor system and/or substrate, with crystallinity, thickness, porosity, flexibility and surface charge control in the thin films.

The use of surfactants as growth controlling agents, to obtain well-ordered WO_3 films with controlled porosity and particle size, has already been reported: cationic surfactants such as hexadecylthymethylammonium bromide (HTAB) [1], anionic surfactants including sodium dodecyl sulfate [2], gemini surfactants [3] as well as nonionic surfactants including poly(alkylene oxide) triblock copolymers such as L62 and P123 [4,5], have been successfully used as templates.

The use of PEG is even more largely reported for obtaining WO_3 films by wet chemical routes, such as dip coating-pyrolysis [6], sol–gel [7,8], or microwave irradiation method [7]. The reports show that PEG can delay crystallization [8,9], allows obtaining stoichiometric films [8] and controls the particle size and shape [10].

Combined surfactant–polyethylene glycol systems as growth and morphology controlling agents are also reported, as the HTAB–PEG combination presented by Deepa and coworkers [11] for the synthesis of WO_3 thin films by electrodeposition. This paper outlines that the HTAB-PEG system improved the ability of the WO_3 to withstand thermal stresses during heating, and enabled the production of well-adherent, free of cracks films.

* Corresponding author.
E-mail addresses: bertus.laura@unitbv.ro (L.M. Bertus), a.duta@unitbv.ro (A. Duta).

0254-0584/$ – see front matter © 2013 Elsevier B.V. All rights reserved.
http://dx.doi.org/10.1016/j.matchemphys.2013.02.047

The interactions expected when using surfactants and PEG in "room temperature" techniques are well established but few reports are commenting on the influence of templating agents in SPD. The interest on this topic rises from the versatility of the SPD technique and its appropriateness for obtaining electrochromic thin films [12,13].

Basically, SPD consists of a pyrolysis reaction, on a heated substrate, of the precursor system dispersed in very small droplets. By adding the surfactant in the precursor system, the surface tension will be lowered, allowing the formation of smaller droplets in the aerosol cone, with consequent modification of the vapor pressure. The extent of this effect depends on the surfactant type (cationic, anionic, non-ionic, zwitteronic) and its characteristics (type and length of the hydrocarbon tail, the position and number of charged groups). Another distinct feature of SPD is the temperature increase in the droplets approaching the substrate that continuously modify the reaction rate.

Further PEG addition in the system will extend the possible interactions and the reactivity control of the tungsten precursor. Therefore, surfactant and PEG addition requires to re-optimize the deposition parameters: the substrate temperature, the break between the spraying sequences – which has to be large enough for allowing the surfactant by-products to eliminate before the next layer is deposited, and the carrier gas pressure for allowing the aerosol to gain enough kinetic energy to reach the substrate before full solvent vaporization and complete reaction of the precursors.

This paper reports on the synthesis of WO_3 thin layers by spray pyrolysis, from a WCl_6 ethanol solution and using, to the best of our knowledge for the first time for this deposition process, a mixture of templating agents consisting of a cationic surfactant (hexadecylthymethylammonium bromide, HTAB) and a nonionic polymer (polyethyleneglycol, PEG400). An interaction mechanism of the WCl_6 inorganic salt with the solvent and templating agents is proposed, to explain the chemistry, surface morphology and charge modifications in the thin films, correlated with their electrochromic activity.

2. Experimental

2.1. Films synthesis

2.1.1. Substrate

Tungsten oxide (WO_3) thin layers were deposited on electrical conductive fluorine-doped tin oxide (FTO, Pilkington, sheet resistance 30 Ω sq^{-1}) using spray pyrolysis. The FTO substrate was cleaned by degreasing with pH neutral detergent, rinsing with deionized water and ultra-sonication in ethanol, followed by drying in compressed air flow.

2.1.2. Precursor solution preparation

The precursor solutions were obtained by dissolving 2.2 g of WCl_6 powder (99.9+%, Acrős Organics) in ethanol (EtOH, 99.2%, P.A.M. Corporation S.R.L), containing acetyl acetone (AcAc, 99%, Alfa Aesar), with WCl_6 and AcAc in a 1:2 M ratio. Hexadecyltrimethylammonium bromide (HTAB) and polyethylene glycol (PEG 400) were added in the spraying solution in the amounts presented in Table 1. A tungsten oxide reference layer was obtained without surfactants addition in the spraying solution.

The properties in the precursor system (conductivity, surface tension) are very much influenced by the different solvation/interaction mechanisms of the WCl_6 inorganic salt in/with the surfactant–ethanol media. Consequently their investigation can help explain the different growth processes occurring in the films and the consequent surface structure, chemistry and morphology. Following this line, the critical micelle concentrations (CMC) of HTAB for all the spraying solutions were evaluated by conductivity measurements (Hanna HI 991200 conductometer). Parallel surface tension stalagmometric measurements were done to confirm the conductivity data.

Table 1
Precursor solution preparation and surface tension values.

Sample	Conc. HTAB [ppm]	WCl_6:PEG400 (w/w)	Surface tension [dyn cm^{-1}]
W	–	–	31.90 ± 0.02
WH1	200	–	30.07 ± 0.02
WH2	500	–	30.22 ± 0.02
WH3	1000	–	29.16 ± 0.02
WHP21	500	2:1	29.61 ± 0.02
WHP11	500	1:1	29.37 ± 0.02
WHP12	500	1:2	28.37 ± 0.02
WP21	–	2:1	26.86 ± 0.02
WP11	–	1:1	29.97 ± 0.02
WP12	–	1:2	29.40 ± 0.02

2.1.3. Deposition conditions

A robotic SPD installation was used, in open atmosphere, with a glass atomizer (Camag, 100 mL). During deposition, the substrate temperature (250 °C), air flow pressure (150 kPa), the spraying angle (45°) and spraying distance (23 cm) were kept constant, as previously optimized [14]. Fifteen consecutive layers were deposited with 100 s break between the spraying sequences. The samples were annealed for six hours at 410 °C for removing the surfactant template and for stabilizing the crystalline structure, followed by rapid cooling down to room temperature.

2.2. Layer characterization

The influence of additives on the crystalline structure and surface morphology of the films were investigated using X-ray diffraction (Advanced D8 Discover Bruker diffractometer, Kα1 = 1.5406 Å, 40 kW, 20 mA, step size 0.02, scan speed 2 s/step, 2θ range from 20 to 60°) and atomic force microscopy (NT-MDT model NTGRA PRIMA EC, semicontact mode with Si-tips, NSG10, force constant 0.15 N m^{-1}, tip radius 10 nm). Roughness was calculated using the AFM software for the 1 μm × 1 μm surface (acceptable error ±0.1 nm).

Surface composition of the initial films was investigated by X-ray photoelectron spectroscopy (VG 220i-XL ESCALAB spectrometer, monochromatic Al Ka excitation, 1486.6 eV) and infrared spectroscopy (Spectrum BX FT-IR System, Perkin Elmer).

The surface energy was estimated based on contact angle measurements (OCA-20 Contact Angle-meter, DataPhysics Instruments, sessile drop mode) at constant room temperature (20 °C). Two testing liquids with different polarity and surface tension (σ_{LV}) were used: glycerol ($\sigma_{L,V}^{20\ °C} = 63.40$ mN m^{-1}) and deionized water ($\sigma_{L,V}^{20\ °C} = 72.80$ mN m^{-1}).

The electrochromic properties of the samples were evaluated by cyclic voltammetry (Voltalab PGP201 potentiostat, scanning rate 10 mV s^{-1}) in a three electrode cell exposed to atmosphere wherein the WO_3-based films act as working electrode, Hg/HgO/KOH 0.1 M as reference electrode and a Pt plate as counter electrode. Bis(trifluoromethane sulfonyl)imide (HTFSI) in butyl-methyl-imidazolium bis(trifluoromethylsulfonyl)-imide (BMITFSI) 0.3 M (Solvionic) was used as electrolyte. Transmission spectra (SECOMAM model UviLine 9400 UV–VIS spectrometer) of the layers in the initial, colored and bleached state were recorded ex situ, with air as reference, in the 330–1000 nm range. For coloration/bleaching times, chronoamperometry experiments were performed in the same setup by applying −0.6 V for 30 s for coloration and +0.6 V for 120 s for

bleaching and transmission was measured in situ (Shimadzu UV–VIS spectrometer) at 550 nm wavelength.

The short range coloration stability of the devices was tested by performing 50–100 coloration–bleaching successive cycles.

3. Results and discussions

3.1. Critical micelle concentration and surface tension measurements

Previous work [14] reported on the CMC of the HTAB surfactant in ethanol–WCl_6 system as being ~1170 ppm for 100 ppm added WCl_6 inorganic salt, which is significantly lower than the concentration in the studies hereby presented. Thus, the CMC of HTAB was re-evaluated, Fig. 1a, while the CMC in systems containing HTAB and PEG400 at the highest amount was evaluated based on the results presented in Fig. 1b.

Tungsten hexachloride dissolves in ethanol by forming an ethoxy chloride complex ($WCl_6 + xC_2H_5OH \rightarrow WCl_{6-x}(OC_2H_5)_x + xHCl$) through partial or total replacement of the Cl^- anions with ethoxy ($C_2H_5O^-$). When the AcAc complexing agent is added a chelate-type compound is formed by (partial) replacement of the ethoxy radicals as shown in Fig. 2a. In the diluted surfactant solutions, below CMC, HTAB monomers are positioned at the solvent surface, with the cationic head directed toward ethanol and the hydrocarbon tale oriented to the gas phase forming a loose layer that is fully stacked when reaching CMC. Likewise, HTAB is possible to group via electrostatic interaction, surrounding the cation "chelate" and developing an electric double layer. The CMC was found to be lower (800 ppm) for higher salt concentration with conductivity having a general decreasing trend characterized by two regimes, before and after CMC (Fig. 1a). With increasing concentration of HTAB the precursor salt ions mobility is limited by their interaction with the positively charged hydrophilic heads of HTAB monomers thus explaining the first decrease in conductivity. When the critical micelle concentration is reached, HTAB starts to aggregate in the ethanol solution, forming spherical oil–water (O/W) micelles. Because of the delocalized negative charge of the six-membered W-chelate rings and the increased charge density at the surface of the micelle, the tungsten complex easily binds to the cationic charged heads of the surfactant (Fig. 2b). The precursor cation trapping in the micelle external layer explains the second decrease in conductivity.

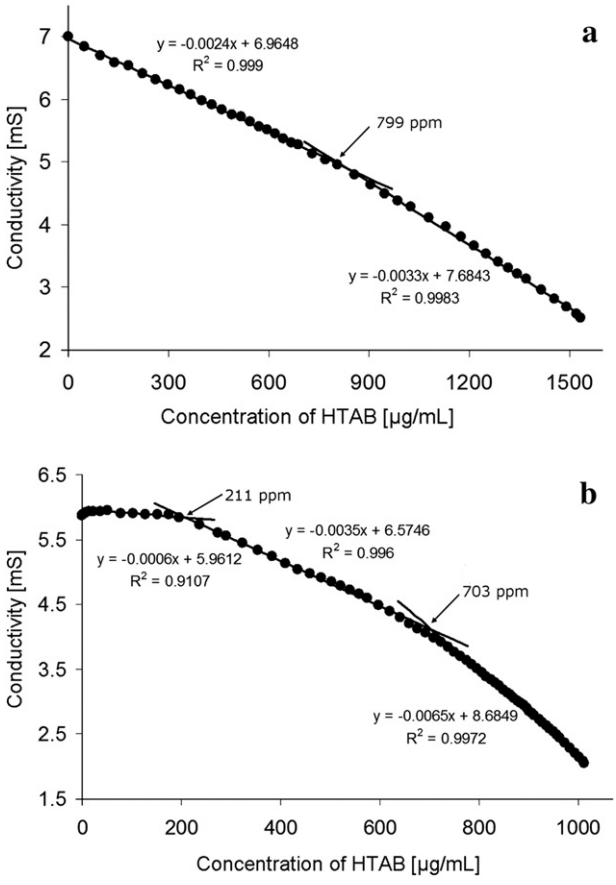

Fig. 1. Critical micelle concentration of the precursor system without (a) and with (b) PEG400.

Previous studies have shown that nonionic polymers can form mixed complexes with cationic surfactants [15] with significant changes in surface tension and viscosity. The surface tension values of all the precursor systems used in SPD are presented in Table 1. In addition, the surface tension of the solutions containing PEG400 (WP21, WP11 and WP12) in the same proportions used for obtaining samples WHP21, WHP11 and WHP12, respectively, without HTAB were investigated to reveal if there is a surfactant–co-surfactant interaction. By adding hexadecyltrimethylammonium bromide (HTAB) in the precursor solution the surface tension decreases, as the surfactant monomers disrupt the hydrogen bonding between the ethanol molecules at the interface. A more obvious decrease in surface tension is observed for higher surfactant concentration (1000 ppm, WH3). As it can be seen in Table 1, addition of PEG400 alone (WP21, WP11 and WP12) had a more significant effect in reducing the surface tension of the solution compared to HTAB (solution WH2).

When PEG400 is added to the solution (WCl_6:PEG400 = 1:2 w/w) two inflection points characterize the conductivity variation (Fig. 1b); the first one could be assigned to the maximum binding concentration (MBC), when PEG400 chains become saturated with HTAB micelles [16,17]. Further addition of surfactant leads to the formation of free micelles in the solution, with a slightly lower micellization point. Most likely, the formation of micelles is lower because of the solvent consumption by PEG400 and free monomers crowding (reduced inter-monomer distances and repulsions) between the surfactant filled polymer coils.

PEG400 has a high hydrophilic character, thus higher affinity toward the ethanol (hydrophilic) media. The adsorption of the polymer chain on the micelles surface is possible through the interaction between the lone electron pair of oxygen atom (hydrogen bond) with the hydrogen atoms of the chelate methyl groups (Fig. 2c). This interaction between the tungsten chelate complex and the polymer increases the biding affinity between PEG400 and HTAB, stabilizing the polymer-surfactant aggregates. Because PEG400 has a rather short length catena, micelles close packing is expected, as the salt reduces the repulsive forces between cationic head groups [16].

The surface tension in solutions containing both the surfactant and the co-surfactant (polymer) system is lower compared to the individual surfactant (HTAB) system; the same effect was registered also in systems containing PEG in higher amounts. The contraction/collapse of the polymer coil is a compensating effect for the increase in the solution viscosity when PEG400 is added, thus explaining the further surface tension decrease (Table 1). The lowest value (28.3 dyn cm^{-1}) was obtained for the highest PEG400 concentration (solution WHP12), confirming the synergic effect obtained in mixing the templating agents.

Considering the long hydrophobic carbon chain (C16) of HTAB, at concentration much higher than the CMC, lamellar micelles can also be formed. At higher polymer concentrations the

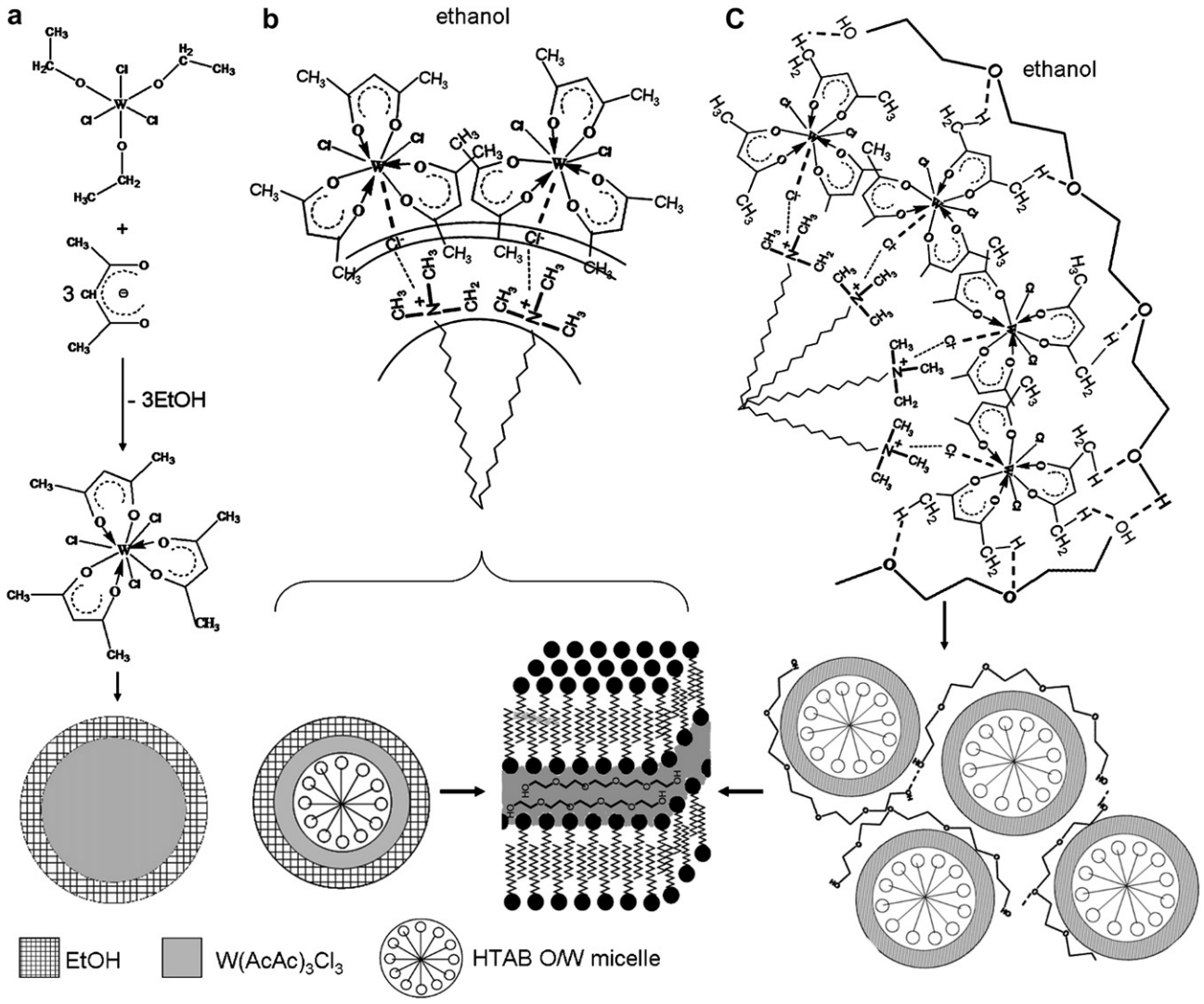

Fig. 2. Simplified model of the different interaction/solvation processes in the precursor systems: (a) WCl_6–AcAc–EtOH, (b) WCl_6–AcAc–HTAB–EtOH and (c) WCl_6–AcAc–HTAB:PEG400–EtOH.

concentration of the ethanol molecules available in the system decreases and phase separation occurs with HTAB micelles self-assembling in the form of liquid crystalline aggregates such as lamellar mesophases with PEG400 hydrophilic chains acting as biding element between the lamellae. As this process is favored by increasing temperature, this lamellar phase is expected to be defined when the precursor reaches the substrate, in the pause between the spraying sequences.

3.1.1. Structural characterization

The XRD patterns of one sample of each group (W, WH2, WHP12) are presented in Fig. 3. All the samples were found to be crystalline. For samples W and WH2 the peak corresponding to the (2 0 0) lattice reflection plane corresponds to 2θ in the range 22–24°, characteristic of the monoclinic structure (JCPDS ICCD 89-4476), suggesting a preferential growth along the (2 0 0) direction, as already reported by Regragui et al. when spraying a solution containing WCl_6 in a 1:1 ethanol:water system onto a substrate heated at 300 °C [18]. Zhang et al. [3] obtained the same crystalline phase for WO_3 films synthesized from a WCl_6–ethanol sol containing a gemini surfactant as template, after annealing at 400 °C for 2 h. The templating role of the lamellar surfactant–polymer aggregates was clearly evidenced in the XRD pattern of sample WHP12, in which the three peaks corresponding to the monoclinic structure (2θ region 22°–25°) are more clearly defined with the (2 0 0) peak having a significantly increased intensity. Peaks corresponding to the substrate were also identified (SnO_2, tetragonal JCPDS ICCD 77-0451) with the highest intensity for W sample probably due to the lower thickness of this layer.

The grain size (D) was calculated using the Scherrer formula, $D = 0.9\lambda/(\mathrm{FWHM}\cdot\cos\theta)$ [19], considering the (2 0 0) peak, where 0.9 is the Scherrer constant, λ is the wavelength of the incident beam, FWHM is the full width at half maximum of the peak and θ is the Bragg angle. The microstrains (ε) were calculated using the Wilson formula $\varepsilon = \mathrm{FWHM}/4\tan\theta$ [20]. The crystallite size and microstrains are presented in the inset of Fig. 3. The increasing values of the crystallites sizes confirm the template assisted mechanisms proposed, with slower nucleation and regular growth, leading to improved crystalline ordering, with lower microstrains.

3.1.2. Morphology and contact angle measurements

As Fig. 4 shows, the layers morphology significantly changes with increasing the surfactants amount, proving the beneficial role of the surfactants in tuning surface properties. As the deposition parameters (substrate temperature, air flow pressure and the configuration of spraying sequences) were kept constant, these

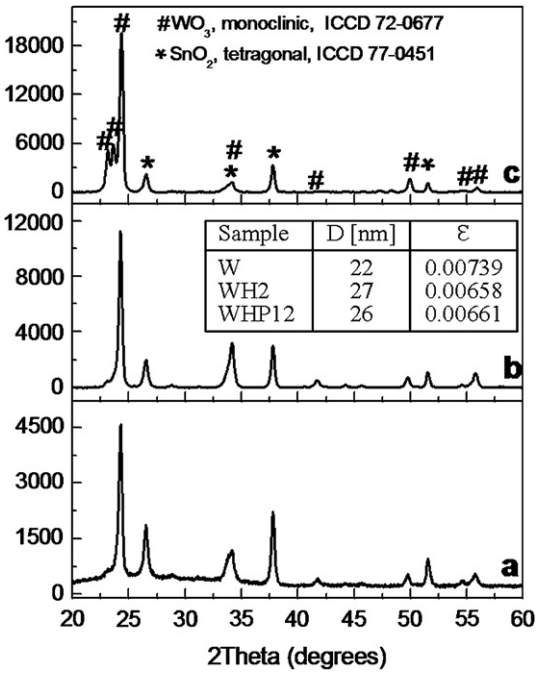

Fig. 3. XRD patterns of the sample W (a), WH2 (b) and WHP12 (c) after annealing at 410 °C.

modifications are only related to the variation in the spraying solution composition, with consequences on the surface tension and consequently vapor pressure.

The reference sample (W) has a granular morphology, with particle size up to 200 nm, well ordered on the surface and closely packed. In this case, the tungsten ion (partially) develops an AcAc-chelate with an ethanol double layer (case a, Fig. 2). The chelate has higher stability than the ethoxychloride complex, with lower reactivity, thus lower nucleation rate that allows forming large particles. Adding HTAB in low concentration (WH1) leads to the formation of homogenous layers with low porosity because, at this surfactant concentration, little interaction between the surfactant monomers and the tungsten chelate is expected. Thus this morphology is mainly the result of changes in solvent surface tension and thus vapor pressure as the monomer forms a loose layer at the surface. As the HTAB concentration is well below CMC most of the surfactant monomers are expected to be stacked at the liquid/vapor (gas) interface with the cationic head directed toward ethanol and the hydrocarbon tale oriented to the gas phase forming a loose layer, lowering the surface tension. Lower surface tension indicates that smaller droplets are formed which according to the Kelvin equation ($\ln(p/p_0) = (2\gamma V_m/rRT)$, p – actual vapor pressure, p_0 – saturated vapor pressure, γ – surface tension, V_m – molar volume, R – universal gas constant, r – droplet radius, T – temperature) corresponds to an increase in the droplet vapor pressure as the pressure inside the droplet is higher than outside. Therefore, in this case smaller droplets and larger in number are directed toward the substrate, with slower evaporation of solvent during the droplet transport as result of the increased vapor pressure, and solvent spreading on the substrate is expected which consequently leads to slower precipitation forming thick dense layers. The solution used for the obtaining the WH2 sample has nearly the same surface tension with the previous one (WH1) meaning that the spraying cone should be formed of approximately the same droplet size and number. The thermal stability of the precursor complex (vapour pressure in the droplet) increases even more and so is the number of monomer–chelate complexes; from these complexes the precursor cation is easily released and more uniformly distributed on the surface leading to more porous layers (case b, Fig. 2). The AFM image (Fig. 4c) shows a textured surface formed of grains randomly distributed on the surface, very different from the previous sample (WH1), proving the role of the micelles template in controlling the thin layer growth.

These results outline that surface tension cannot represent a sole criteria in predicting the morphology and, approaching CCM, reactivity variations can and must be considered. Above the CCM (sample WH3) the micelles that reach the substrate can undergo coalescence as result of a significant decrease in the solvent concentration (by evaporation), forming liquid crystalline lamellar structures. The resulting morphology (Fig. 4d), a textured surface with no clearly defined particles and large pores, might be the result of high thermal stress within the film, generated when removing the solvent trapped between the hydrophobic domains of the lamellae, which might cause the structure to collapse during calcinations at 410 °C.

In salt containing systems, the number of bound HTAB molecules per chain is expected to increase [18], i.e. the added salt stabilizes the binding of HTAB micelles to the polymer and thus the aggregates, avoiding the collapse of the template structure during annealing. This explains the morphology regularization with PEG addition, sample WHP12 (Fig. 4g), being the most homogenous. The lamellar template is even more likely in samples obtained by adding HTAB-PEG 400 mixtures, because the hydrophilic polymer has the tendency to trap the ethanol molecules supporting phase separation.

As Fig. 4e–g shows, by modifying the PEG 400 concentration the size of the resulting particles could be controlled. When PEG wraps the micelles (Fig. 2c) the size of the aggregates is increased leading to the formation of larger particles (sample WHP21). However, with increasing PEG concentration the hydrodynamic volume of PEG-HTAB aggregates is reduced due to effects of polymer chain contraction via the electrostatic screening [17] explaining the decrease in the particle sizes from up to 300 nm (sample WHP21) to approximately 150 nm (sample WHP12).

The wetting behavior of WO_3 thin layers is influenced by surface roughness, surface chemistry, surface energy and homogeneity. Surface free energies (σ^{SL}) and their dispersive (σ^D) and polar (σ^P) components were calculated by subtracting the geometric mean of both polar and dispersive contributions according to the Owens–Wendt–Rabel and Kaelble equation [21]:

$$\frac{(1+\cos\theta)\cdot\sigma_L}{2\sqrt{\sigma_L^D}} = \sqrt{\sigma_S^P\cdot\frac{\sigma_L^P}{\sigma_L^D}} + \sqrt{\sigma_S^D} \quad (1)$$

where σ_L^D and σ_L^P represent the dispersive and polar parts of the liquid, σ_S^D and σ_S^P represent the respective contributions of the solid and θ is the contact angle of the testing liquids on the substrates.

The contact angle values recorded at the initial moment of the drop-film contact for water and glycerol are presented in Table 2, along with the surface energies. The data prove the hydrophilic character, as the polar component has always the largest share in the surface energy, as expected for an oxide. The low contact angles values also indicate the presence of polar functional groups such as –OH that can form hydrogen bonds with water molecules allowing the water penetration within the film. The adsorption of water at the film surface from atmosphere is also possible especially for porous layers. Likewise, if the orientation of surfactant template for the last deposited layer is with the polar head toward the surface the result will be an increased water bonding and thus an increase in water-wettability.

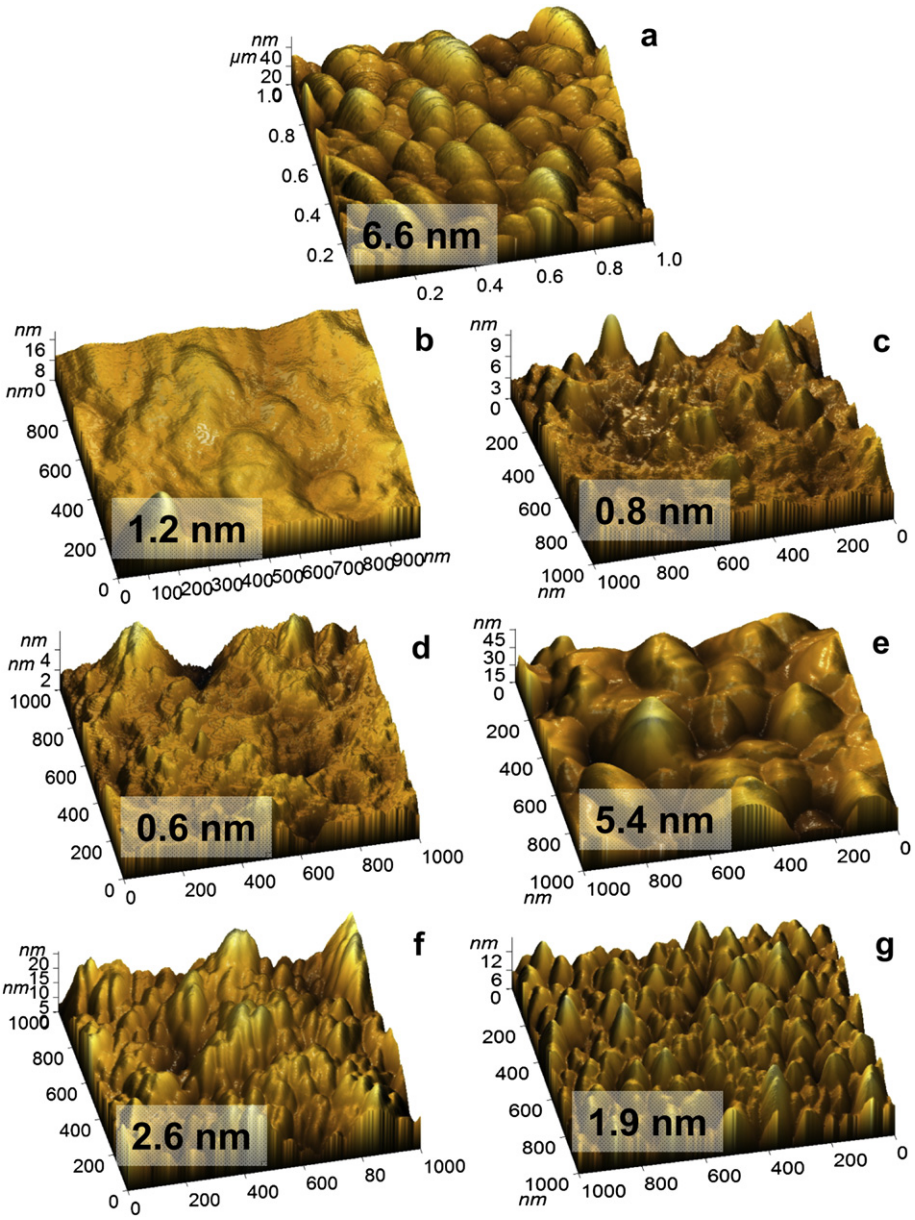

Fig. 4. AFM images (3D, 1 μm × 1 μm) of the samples W (a), WH1 (b), WH2 (c), WH3 (d), WHP21 (e), WHP11 (f) and WHP12 (g).

The variation of the contact angle during a 100 s contact time is linear and almost constant, proving fast adsorption. The slopes of the contact angle variation in time is almost constant, regardless the substrate, in good agreement with the roughness low values, Fig. 5.

Table 2
Contact angle measurements results for water and glycerol for the obtained films.

Sample	Contact angle, θ (°)		Surface energy σ_S (mN m^{-1})	Dispersive component σ^D (mN m^{-1})	Polar component σ^P (mN m^{-1})
	Water	Glycerol			
W	46	62	94.05	0.18	93.86
WH1	35	45	79.97	2.24	77.73
WH2	40	40	60.15	10.66	49.49
WH3	26	45	103.35	0.14	103.21
WHP11	31	46	90.52	0.84	89.69
WHP12	31	45	87.83	1.14	86.69
WHP21	30	45	90.98	0.94	90.04

The addition of surfactants increases the surface charge of the WO_3 thin films as confirmed by the lower values of the water contact angles. The results also show that the surface energy variation can be mainly linked with the surface topology (rounded, as in the W and WH1 samples or fractured, with large pores, as in WH3). Samples WHP21, WHP11 and WHP12 have almost similar surface energies although they are not characterized by the same morphology or roughness, indicating that surface chemistry has the major role in the wetting behavior. These results also show that the PEG addition has a "leveling" effect in terms of surface charge. The control of the hydrophilic behavior is important considering the further use of the layers, in direct contact with electrolytes, in the electrochromic devices.

For further analysis three samples were selected, W, WH2 and WHP12, having different precursors compositions, different morphologies, dissimilar hydrophilic character, high crystallinity and high initial transmittance, as requested for electrochromic applications.

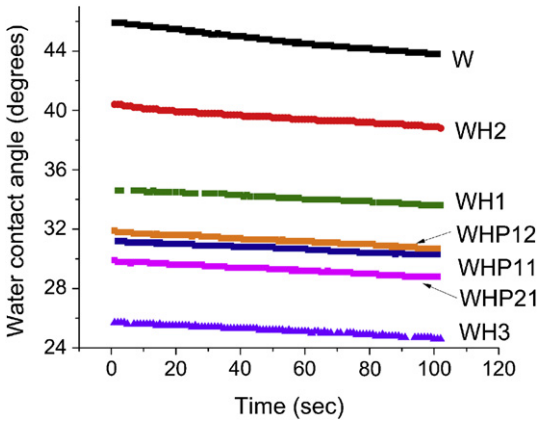

Fig. 5. Water contact angle evolution with time for the samples.

3.1.3. Surface composition

Direct experimental proof of the water adsorbed/absorbed in the films was obtained from the FTIR spectra (Fig. 6) by the broad adsorption band in the 1100–3500 cm^{-1} region [22] which increases in intensity for samples WH2 and WHP12, and by the weak band at 1420 cm^{-1} corresponding to the δ (OH) bending vibration [23]. The bands centered at 792 and 710 cm^{-1} correspond to the υ (W–O_{intra}–W) stretching vibration of the bridging oxygen [24,25]. The band at 890 cm^{-1} has earlier been observed at 900 cm^{-1} and at 898 cm^{-1} by M. Deepa et al. [26] and corresponds to the combined effect of υ (O–O) stretching vibration of the peroxo group and υ (W–O_{inter}–W) stretching of the bridging oxygens. Similar bands were observed in monoclinic tungsten oxide (706, 813 and 890 cm^{-1}) and confirmed by Raman spectra by A. Rougier et al. [27]. With surfactant addition (sample WH2) these bands are shifted to higher wave numbers (716 and 902 cm^{-1}) as result of changes in the film composition i.e. hydrogen bonding with surrounding water but also in film structure. For sample WHP12 the band at 716 cm^{-1} is also present while the band corresponding to the υ (O–O) and υ (W–O_{inter}–W) stretching vibrations is shifted to lower wavenumbers (880 cm^{-1}) and so is the band corresponding υ (W–O_{intra}–W) stretching vibration (800 cm^{-1}) suggesting strong networking via oxygen atoms and water molecules. In addition, for sample WHP12 we observe an extra band centered at 846 cm^{-1} assigned also to the W–O–W in monoclinic tungsten oxide [28]. No bands corresponding to surfactant by-products could be identified,

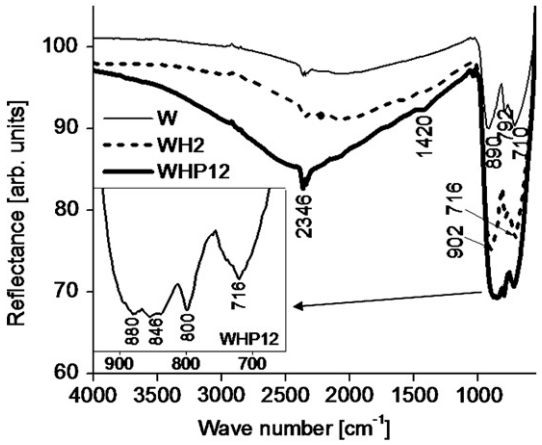

Fig. 6. FTIR spectra of the samples W, WH2 and WHP12; zoom of the 500–1000 cm^{-1} region for sample WHP12 in the inset.

confirming that the appropriate deposition temperature (250 °C) has been selected after optimization [29], allowing complete by-products decomposition as compared to our previous attempt [14] when the substrate temperature was too low (200 °C). The increasing amounts of water on film surface are in good agreement with the contact angle results and outline the high moisture sensitivity of these films.

The XPS high-resolution spectra of W 4f and O 1s core levels for the WO_3 thin films are presented in Fig. 7a and b, respectively. For sample W the binding energies of $W^{6+}4f_{5/2}$ and $W^{6+}4f_{7/2}$ levels are observed at 37.9 and 35.7 eV respectively, with a spin-orbit separation of 2.14 eV and $W^{6+}4f_{5/2}/W^{6+}4f_{7/2}$ ratio of 0.76–0.77. The energy position of the doublet is in agreement with the XPS data reported in literature [3,30],. In addition, for sample WH2 the presence of W^{5+} states was evidenced with $W^{5+}4f_{5/2}$ and $W^{5+}4f_{7/2}$ levels located at 36.8 and 34.6 eV respectively. The content of W^{5+} is lower than 5%.

The low values of the FWHM, 0.98–1.0 for the $W^{6+}4f_{7/2}$ level and 0.97–1.02 eV for $W^{6+}4f_{5/2}$ level, point out the crystallinity of the samples. The O1s peak was deconvoluted in four components. Component **I** with a binding energy of 530.6 eV is assigned to the oxygen atoms (O^{2-}) that form the strong W=O bonds [31]. Component **II** at 531.4 eV corresponds to OH-groups [32,33], and possibly to C=O groups, whereas the third (**III**) component located at 532.2 eV illustrates the C contamination and is more precisely attributed to C–O bonds [32]. The highest energy peak (component **IV**, 533.2 eV) is attributed to water bound at the surface of the samples [34], proving the existence at the surface of $WO_3(H_2O)_n$-phases. The chemisorbed water decomposes under annealing into –OH groups of which contribution is found in component II. This surface contamination may have occurred during annealing and cooling sequences when water or C_{Hx} pollution and its oxidized forms could have been easily adsorbed to the surface of the porous samples. As the FTIR spectra do not show peaks corresponding to surfactant decomposition, we assume that the contribution of C–O or C=O bonds is small.

3.1.4. Electrochromic properties

The electrochemical characterization was performed in a non-aqueous viscous electrolyte (HTFSI in BMITFSI 0.3 M). The current–voltage characteristics for the second cycle are presented in Fig. 8a.

Coloration and bleaching charges (Q_c and Q_b) were calculated by integrating the respective areas of the C–V curves and the results are presented in Table 3. At a fixed potential of –0.6 V, the magnitude of reduction and oxidation currents and consequently the coloration/bleaching charges reached the highest values for the WH2 sample. The morphology of sample WH2 i.e. sharp edgy particles interconnected by large open pores provides a better film–electrolyte interface contact as compared to sample W formed of rounded particles closely packed or sample WHP12 with particles as sharp as sample WH2 but much smaller pores. This suggests that when using viscous electrolytes a surface structure similar with sample WH2 facilitates the ions diffusion.

The result emphasizes the importance of pore dimensions and particle shape in coloration/bleaching processes especially when using viscous organic electrolytes in which ion diffusion is by far smaller compared to aqueous electrolytes. For the WHP12 film the overall flattening of the oxidation peak in the cyclic voltammograms indicate slower kinetics in the bleaching/coloring process. For samples W and WHP12 lower coloration charges compared to sample WH2 were obtained as a possible result of their closely packed structure. The higher reduction capacity originates from the side reactions, such as hydrogen evolution ($2H^+ + 2e^- \rightarrow H_2$), when going down to –0.6 V. The small cathodic peak at about 0 V

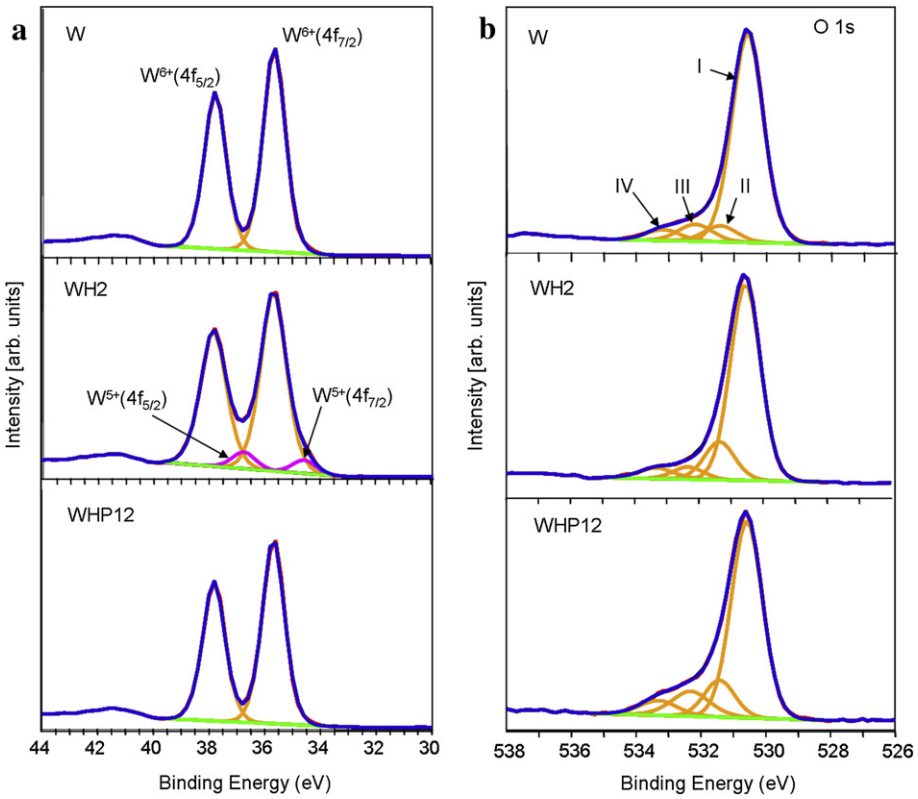

Fig. 7. XPS spectra of W4f (a) and O1s-levels (b) of the samples W, WH2 and WHP12.

gradually disappears after performing multiple cycles, indicating surface charge transfer irreversible reactions. The potential needed for bleaching the films is rather high (−1.2 V) and the transmission reaches higher values than for the initial state, again suggesting that either film dissolution or film conditioning might occur.

The transmission spectra of samples W, WH2 and WHP12 within the 350–1000 nm wavelength range for the virgin, colored and bleached states are illustrated in Fig. 8b.

The film thickness was calculated from reflectance spectra using the relation:

$$d = \frac{\lambda_1 \lambda_2}{2(\lambda_2 - \lambda_1)(n_1^2 - \sin^2 \alpha)} \quad (2)$$

where λ_1 and λ_2 are the wavelength of two consecutive maxima, n is the refractive index of WO_3 (1.7, [14]) and α is light incidence angle (6°). Results are given in Table 3.

Samples W and WH2 have noticeably lower transmission in the initial state compared to WHP12 sample, which will definitely limit their use in electrochromic applications. So using the surfactant improves the transmission in the initial state of the films without significant modification in the film thickness.

The coloration efficiency (η) defined as the attenuation in the transmitted light during colored and bleached states per charge density ($\eta = \Delta OD/Q = 1/Q \log T_b/T_c$), the transmittance modulation ($\Delta T = T_b - T_c$) and the contrast (T_b/T_c) were calculated for the 2nd and after multiple cycles, at the 550 nm wavelength, and the results are presented in Table 3. The number of exchanged electrons x (number of intercalated H^+ ions) was calculated using the formula [35]:

$$x = (Q_c/96,500) \times (M/m) \quad (3)$$

where Q_c is the coloration charge, M was taken as the WO_3 molecular weight, and m is the weight of the film and given by:

$$m = \rho \times d \times s \quad (4)$$

Film density was considered 75% of the bulk WO_3 ($\rho = 5.76$ g cm^{-2}). Results are shown in Table 3, however the values are only preliminary, as the film density may increase along with crystallinity, i.e. W < WH2 < WHP12, according to XRD data. Of course, the porosity factor has to be considered also when trying to correlate these values with the coloration efficiency.

The optical modulation and coloration efficiency reached the highest values for the WHP12 film, 38% and 31.5 cm^2 C^{-1}, respectively, although is characterized by the lowest value for protons intercalation ($x = 0.17$). The inferior values of the electrochromic parameters obtained for samples W and WH2 can be related to the reduced transparency in the initial state (Fig. 8b) and thus in the bleached state. For sample WH2 the lower coloration might be explained by the presence of W^{5+} states, as shown by XPS analysis. The transmission vs. time transients at 550 nm when the potential of the working electrode was switched between −0.6 V (30 s) and +0.6 V (120 s) are shown in Fig. 8c. Coloration and bleaching times were calculated as the time required for achieving 90% of the total transmission change. Surface morphology not only influences the charge capacity but also the coloration/bleaching kinetics. Bleaching being a diffusion-controlled process is more sensitive to the microstructure of the layers than coloration [36]. So the observed slower bleaching times for samples W and WHP12 compared to sample WH2 (shortest bleaching time) can also be attributed to the observed modifications in the film microstructure brought about by the template. It was already reported that higher coloration and bleaching times are needed for films with granular morphology compared to one-dimensional (1D) nanostructures [11,37,38] as the late ones provide higher surface area.

The EC performance of different WO_3 thin layers obtained by SPD is presented in Table 4. Comparing the EC efficiency with other reported results is difficult as the EC properties of the WO_3 layers in

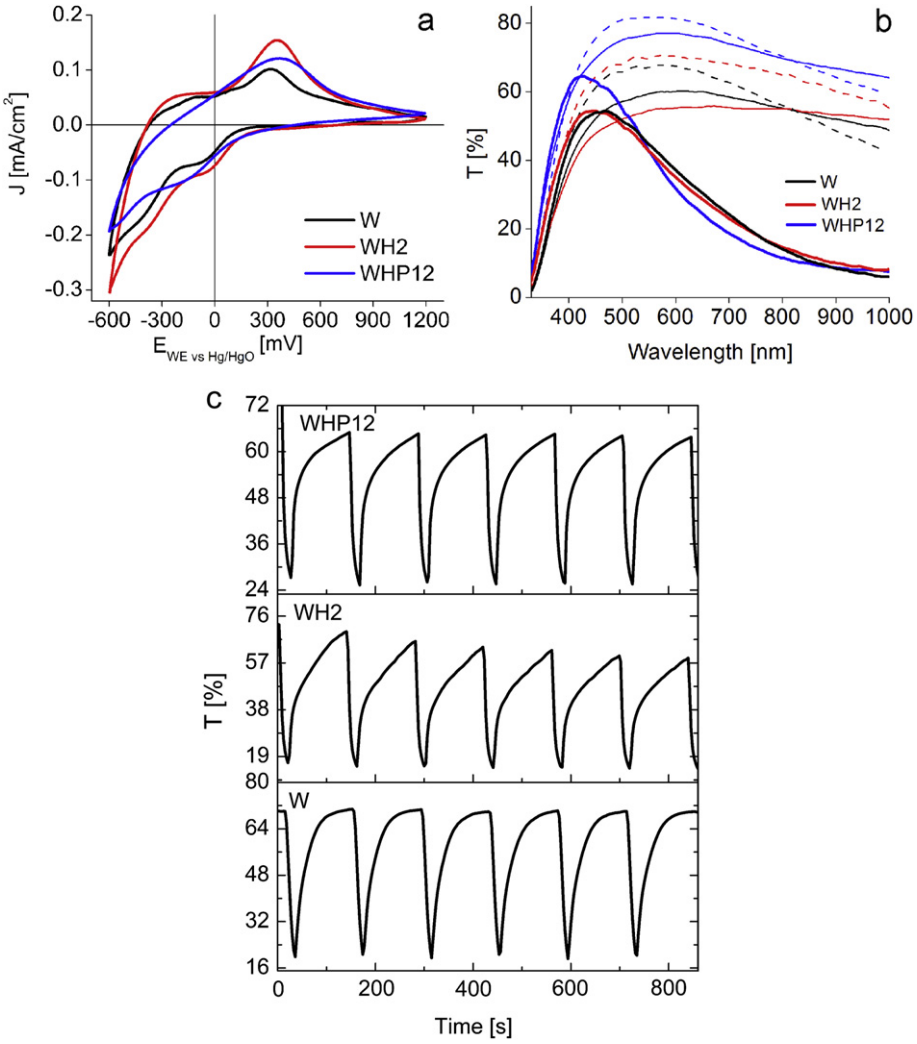

Fig. 8. Current–voltage curves (a), transmission spectra in the initial (smooth line), colored (thicker smooth line) and bleached (dotted line) state (b) and transmission vs. time (c) for samples W, WH2 and WHP12.

this ionic liquid electrolyte were not tested before and the scanning electrochemical parameters and film properties (thickness and morphology) are different from the ones reported. There are few reports of EC properties for WO_3 thin films obtained by SPD and for those reported the electrochemical testing was mostly done in aqueous acidic solution and cycling stability was not tested.

The CE values for the samples reported by the same group [29] or others [40,41] for the WO_3 films tested in aqueous electrolytes are higher than those of sample W tested in the ionic liquid. This is because the diffusion is slower in the viscous ionic liquid compared to the aqueous H_2SO_4 as confirmed also by the coloration/bleaching times i.e. 13 s/58 s and 5–5.5 s/3–3.8 s [40,41], respectively. However, lower contrast [40,41] was obtained compared to any of the samples referred to in this study, suggesting that bleaching was not reversible. By using the right combination of surfactants (sample WHP12) both CE and ΔT higher values can be obtained when cycling in HTFSI-BMITFSI 0.3 M as opposed to aqueous electrolytes. The highest CE value (47 cm^2 C [42]) was reported for WO_3 films cycled in 0.5 M $LiClO_4$-PC, higher than for any of the samples tested in HTFSI-BMITFSI 0.3 M, but there is no information about the contrast or the reversibility of the coloration process.

Fig. 9 shows the change of the CV curve and the coloration and bleaching charges (in the inset) after multiple coloration–bleaching cycles (50–100 cycles) between −0.6–1.2 V.

Table 3
Electrochemical and electrochromic parameters of the W, WH2 and WHP12 samples for the 2nd and for 50–100 cycles (in the brackets).

Sample	d [nm]	Q_c [mC cm^{-2}]	Q_b [mC cm^{-2}]	x	$\Delta T_{550\ nm}$ [%]	$CE_{550\ nm}$ [cm^2 C^{-1}]	Contrast [T_b/T_c]	t_c [s]	t_b [s]
W	347	9.9	7.9	0.20	23	18.4	1.5	13.0	58.2
		(9.6)	(9.2)	(0.19)	(13)	(10.2)	(1.2)		
WH2	372	11.3	9.8	0.21	27	19.0	1.5	18.5	46.7
		(12.5)	(11.2)	(0.24)	(30)	(21.5)	(1.8)		
WHP12	370	8.8	7.8	0.17	38	31.5	1.9	18.8	50.5
		(5.6)	(5.3)	(0.10)	(35)	(43.0)	(1.7)		

Table 4
EC performance comparison between WO_3 thin layers obtained by spray pyrolysis deposition.

Precursor solution	Electrolyte	d [nm]	ΔT [%]	CE [$cm^2\ C^{-1}$]	t_c/t_b [$s\ s^{-1}$]
Aq. ammonium tungstate [40]	0.001 M H_2SO_4	n/a	8	26	5.0/3.0
WCl_6–AcAc–EtOH [29]	1 M H_2SO_4	180	53	21	n/a
	CH_3COOH–CH_3COONa pH = 4 buffer	180	30	24	n/a
WCl_6–EtOH:H_2O (1:1) [18]	0.5 M H_2SO_4	150	30	n/a	n/a
Aq. ammonium tungstate [41]	H_2SO_4	500	10	34	5.5/3.8
Aq. ammonium tungstate [42]	0.5 M $LiClO_4$-PC	500	n/a	47	n/a

Aq. – aqueous, t_c/t_b – coloration/bleaching time.

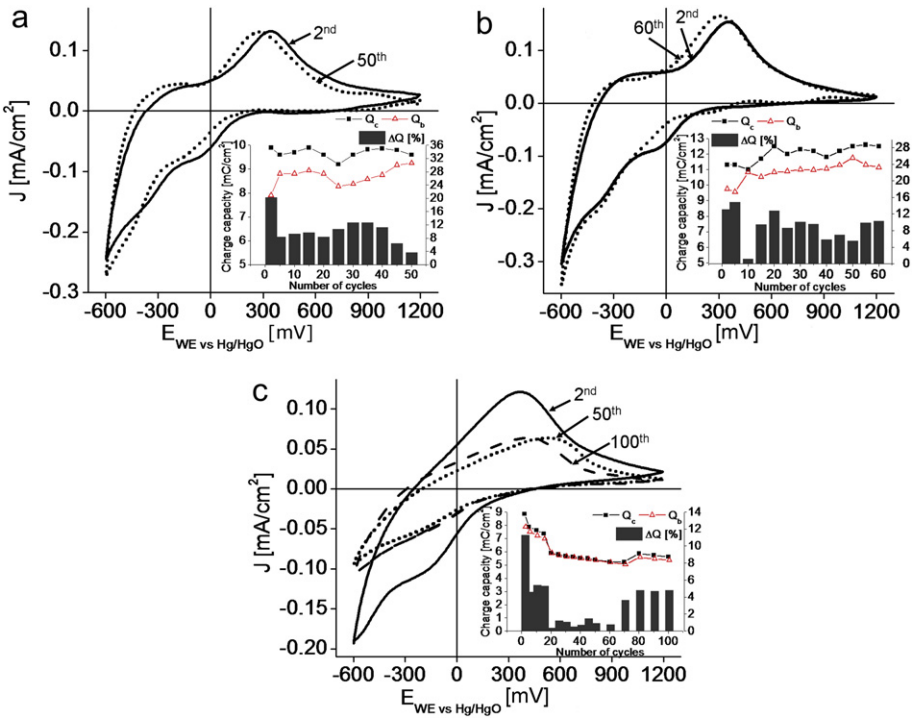

Fig. 9. Current–voltage curves, coloration, bleaching and uncompensated charges evolution (in the insets) with the number of cycles for samples W (a), WH2 (b) and WHP12 (c).

The uncompensated charge was calculated ($\Delta Q[\%] = (Q_c - Q_b) \bullet 100/Q_c$) and plotted vs. the number of cycles (Fig. 9a–c, insets).

For samples W and WH2 the position of the anodic peak is slightly shifted negatively and the cathodic current increases (Fig. 9 a and b, respectively) after 50 and 60 cycles, respectively. The CE, ΔT and contrast of sample W decrease after 50 cycles (Table 4) due to irreversibility of the coloration–bleaching process as confirmed by the values of the uncompensated charge which vary from 20.2% for the 2nd cycle to 3.6% for the 50th cycle (inset of Fig. 9a). This poor reversibility might be caused by layer dissolution as consequence of poor adherence to the substrate. In contrast, the CE and ΔT for sample WH2 have a minor increase which is well correlated with the increase in the number of exchanged electrons and in the coloration and bleaching charges (inset of Fig. 9b), suggesting that the film might undergo formatting. For sample WHP12 a severe change in the CV shape is observed (Fig. 9c) with increasing the number of cycles. Although the uncompensated charge for the last 20 cycles remained unchanged (~4.5%, inset of Fig. 9c) the coloration efficiency is increased (43 $cm^2\ C^{-1}$) as the coloration charge decreases from 8.8 mC cm^{-2} for the 2nd cycle to 5.6 mC cm^{-2} for the 100th cycle.

The use of the HTAB-PEG400 template, enhanced the crystalline order and layer surface area, increased water concentration at the surface with a positive effect as already reported [36,39], all these being responsible for the higher reversibility (low uncompensated charge). Further testing of this film during more cycles will tell us if the first 100 cycles are part of film conditioning and will give information about the long term cycling stability.

3.2. Conclusions

Very smooth and homogenous tungsten oxide layers with monoclinic structure were obtained by spray pyrolysis deposition using a cationic surfactant (HTAB) and polymer–surfactant (PEG400-HTAB) mixtures as templates, after annealing at 410 °C. The addition of surfactants modifies the surface tension of the spraying solution, influencing the nucleation and growth processes and thus the properties of the films. An interaction mechanism of the WCl_6 inorganic salt with the complex system formed by the surfactant (HTAB), co-surfactant (PEG400) and ethanol was proposed for the first time and used to explain these changes. Crystallites' size and the aggregates formation can be tuned by modifying the PEG400-HTAB ratio, with particles ranging from 150 to 300 nm in layers with various topologies. Surface analysis shows a hydrophilic character and the water/moisture sensitivity of the films, correlated with the morphology and chemistry of the layers. The electrochromic activity of the WO_3 films can be improved by using the HTAB-PEG400 templating system.

Acknowledgments

This work was supported by the Sectoral Operational Programme Human Resources Development (SOP HRD), ID59321, financed from the European Social Fund and by the Romanian Government.

References

[1] N. Asim, S. Radiman, M.A. Yarmo, J. Appl. Sci. 6 (7) (2009) 1424–1428.
[2] M. Deepa, A.K. Srivastava, S.A. Agnihotry, Acta Mater. 54 (2006) 4583–4595.
[3] Y. Zhang, Jiaguo Yuan, Jun Le, Lixin Song, Xingfang Hu, Sol. Energy Mater. Sol. Cells 93 (2009) 1338–1344.
[4] W.H. Lai, J. Shieh, L.G. Teoh, I.M. Hung, C.S. Liao, M.H. Hon, J. Alloys Compd. 396 (2005) 295–301.
[5] W.H. Lai, L.G. Teoh, Yen Hsun Su, Jiann Shieh, Min Hsiung Hon, J. Alloys Compd. 438 (2007) 247–252.
[6] H. Yang, F. Shang, L. Gao, H. Han, Appl. Surf. Sci. 253 (2007) 5553–5557.
[7] K. Kajihara, N. Nakanishi, K. Tanaka, K. Hirco, N. Soga, J. Am. Ceram. Soc. 81 (1998) 2670–2676.
[8] V. Hariharan, S. Radhakrishnan, M. Parthibavarman, R. Dhilipkumar, C. Sekar, Talanta 85 (2011) 2166–2174.
[9] Xiangcun Li, Gaohong He, Gongkui Xiao, Hongjing Liu, Mei Wang, J. Colloid Interface Sci. 333 (2009) 465–473.
[10] M. Deepa, M. Kar, D.P. Singh, A.K. Srivastava, Shahzada Ahmad, Sol. Energy Mater. Sol. Cells 92 (2008) 170–178.
[11] M. Deepa, A.K. Srivastava, S. Lauterbach, Govind, S.M. Shivaprasad, K.N. Sood, Acta Mater. 55 (2007) 247–255.
[12] C.G. Granqvist, Electrochromic devices, J. Eur. Ceram. Soc. 25 (12) (2005) 2907–2912.
[13] C.G. Granqvist, Sol. Energy Mater. Sol. Cells 99 (2012) 1–13.
[14] L.M. Bertus, A. Duta, Ceram. Int. 38 (2012) 2873–2882.
[15] S. Suksamranchit, A. Sirivat, A.M. Jamieson, J. Colloid Interface Sci. 294 (2006) 212–221.
[16] K.Y. Mya, A. Sirvat, A.M. Jamieson, J. Phys. Chem. B 107 (2003) 5460–5466.
[17] S. Suksamranchit, A. Sirivat, Chem. Eng. J. 128 (2007) 11–20.
[18] M. Regragui, M. Addou, A. Outzourhit, J.C. Bernéde, Elb El Idrissi, E. Benseddik, A. Kachouane, Thin Solid Films 358 (2000) 40–45.
[19] G. Sui, W.H. Zhong, X. Ren, X.Q. Wang, X.P. Yang, Mater. Chem. Phys. 115 (2009) 404–412.
[20] A.K. Singh, C. Balasingh, J. Appl. Phys. 90 (2001) 2296–2302.
[21] C. Valduta, L. Andronic, M. Visa, A. Duta, Surf. Coat. Technol. 202 (2008) 2448–2452.
[22] N. Sharma, M. Deepa, P. Varshney, S.A. Agnihotry, Thin Solid Films 401 (2001) 45–51.
[23] G. Leftheriotis, S. Papaefthimiou, P. Yianoulis, Sol. Energy Mater. Sol. Cells 83 (2004) 115–124.
[24] F. Daniel, B. Desbat, J.C. Lassegues, B. Gerand, M. Figlarz, J. Solid State Chem. 67 (1987) 235–247.
[25] T. Ivanova, K.A. Gesheva, G. Popkirov, M. Ganchev, E. Tzvetkova, Mat. Sci. Eng. B 119 (2005) 232–239.
[26] M. Deepa, M. Kar, S.A. Agnihotry, Thin Solid Films 468 (2004) 32–42.
[27] A. Rougier, F. Portemer, A. Quédé, M.El. Marssi, Appl. Surf. Sci. 153 (1999) 1–9.
[28] J. Pfeifer, C. Guifang, P. Tekula-Buxbaum, B.A. Kiss, M. Farkas-Jahnke, K. Vadasdi, J. Solid State Chem. 119 (1995) 90–97.
[29] L.M. Bertus, A. Enesca, A. Duta, Thin Solid Films 520 (2012) 4282–4290.
[30] G. Leftheriotis, S. Papaefthimiou, P. Yianoulis, A. Siokou, Thin Solid Films 384 (2001) 298–306.
[31] R. Cardenas, J. Torres, J.E. Alfonso, Thin Solid Films 478 (2005) 146–151.
[32] R. Azimirad, N. Naseri, O. Akhavan, A.Z. Moshfegh, J. Phys. D Appl. Phys. 40 (2007) 1134–1137.
[33] J. Clatot, G. Campet, A. Zeinert, C. Labrugere, M. Nistor, A. Rougier, Sol. Energy Mater. Sol. Cells 95 (2011) 2357–2362.
[34] A.P. Shpak, A.M. Korduban, M.M. Medvedskij, V.O. Kandyba, J. Electron. Spectrosc. Relat. Phenom. 156–158 (2007) 172–175.
[35] A. Rougier, K. Sauvet, L. Sauques, Ionics 14 (2008) 99–105.
[36] C.G. Granqvist, Handbook of Inorganic Electrochromic Materials, Elsevier, New York, 1995.
[37] C.-C. Liao, F.R. Chen, J.J. Kai, Sol. Energy Mater. Sol. Cells 91 (2007) 1258–1266.
[38] J.M. Wang, E. Khoo, P.S. Lee, J. Ma, J. Phys. Chem. C 112 (2008) 14306–14312.
[39] A. Cremonesi, D. Bersani, P.P. Lottici, Y. Djaoued, P.V. Ashrit, J. Non-Cryst. Solids 345–346 (2004) 500–504.
[40] S.R. Bathe, P.S. Patil, Solid State Ionics 179 (2008) 314–323.
[41] S.R. Bathe, P.S. Patil, Sol. Energy Mater. Sol. Cells 91 (2007) 1097–1101.
[42] A.K. Bhosale, N.I. Tawal, P.S. Shinde, P.M. Kadam, R.S. Patil, S.R. Barman, P.S. Patil, Solid State Ionics 180 (2009) 1324–1331.